

Development of Low-Cost DDGS-Based Activated Carbons and Their Applications in Environmental Remediation and High-Performance Electrodes for Supercapacitors

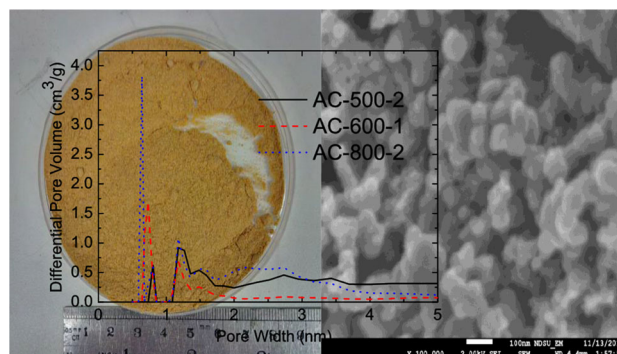
Yong Wang^{1,2} · Jian Zhou³ · Long Jiang^{1,2} · Chad Ulven¹ · Gilles Lubineau³ · Guodong Liu⁴ · Jianchao Xiao⁵

Published online: 28 August 2015
© Springer Science+Business Media New York 2015

Abstract A one-step, facile method to produce 3-dimensional porous activated carbons (ACs) from corn residual dried distillers grains with solubles (DDGS) by microwave-assisted chemical activation was developed. The ACs' application potentials in dye removal and supercapacitor electrodes were also demonstrated. The porous structure and surface properties of the ACs were characterized by N₂ adsorption/desorption isotherms and scanning electron microscopy. The results showed that the surface area of the as-prepared ACs was up to 1000 m²/g. In the dye removal tests, these DDGS-based ACs exhibited a maximum adsorption ratio of 477 mg/g on methylene blue. In electric double layer capacitors, electrochemical tests indicated that the ACs had ideal capacitive and reversible behaviors and exhibited excellent electrochemical performance. The specific capacitance varied between 120 and 210 F/g under different scan rates and current densities. In addition, the capacitors showed excellent

stability even after one thousand charge–discharge cycles. The specific capacitance was further increased up to 300 F/g by in situ synthesis of MnO₂ particles in the ACs to induce pseudo-capacitance. This research showed that the DDGS-based ACs had great potentials in environmental remediation and energy storage applications.

Graphical Abstract



✉ Long Jiang
long.jiang@nds.edu

✉ Gilles Lubineau
gilles.lubineau@kaust.edu.sa

¹ Department of Mechanical Engineering, North Dakota State University, Fargo, ND 58108, USA

² Program of Materials and Nanotechnology, North Dakota State University, Fargo, ND 58108, USA

³ COHMAS Laboratory, Physical Sciences and Engineering Division, King Abdullah University of Science and Technology (KAUST), Thuwal 23955-6900, Saudi Arabia

⁴ Department of Chemistry and Biochemistry, North Dakota State University, Fargo, ND 58108, USA

⁵ Department of Industrial and Manufacturing Engineering, North Dakota State University, Fargo, ND 58108, USA

Keywords Biomass · DDGS · Activated carbon · Adsorption · Energy storage · Supercapacitors · Electrodes

Introduction

Dried Distillers Grains with Solubles (DDGS) is the primary by-product from dry-milled corn ethanol production. Each year the US produces 14 billion gallons of corn ethanol and as a result 30 million tons of DDGS is generated [1]. DDGS typically contains about 42 % fiber, 27 % crude protein, 7 % starch, and 0.6 % phosphorus [2], and is primarily used as an animal feed. Due to its large yield, the value of DDGS is fairly low, selling at less than

10 cents/lb in bulk. It is therefore important to find new value-added uses for DDGS to increase the sustainability of the corn ethanol industry.

One potential use of DDGS is to produce activated carbons (ACs), which are carbonaceous materials with high specific surface area, microporous structure and various surface functional groups. ACs can be produced using different activation methods and activation agents. The specific surface area of ACs measured by Brunauer–Emmett–Teller (BET) method typically ranges from 1000 to 2000 m²/g. Due to their high specific surface area, high thermal stability, relatively low cost, wide availability and strong adsorption capability, ACs have been widely used to remove heavy metals [3] and dyes [4] from liquids. Various techniques, including physical, chemical and biological methods, and their combinations, have been investigated for color removal from dye-laden wastewater [5]. Among these techniques, the physical adsorption by ACs is considered to be a simple, low-cost and effective method [6].

Another important use of ACs is to make electrodes for energy storage devices such as batteries and capacitors. Electric double layer capacitors (EDLCs) are widely recognized as an alternative to batteries with the advantages of high power density, large capacity, relatively low leakage current, long cycle life and simple charge–discharge mechanisms [7]. As a result, EDLCs have played an increasingly important role in energy storage applications. The electrodes in an EDLC show significant effects on the electrochemical properties of the supercapacitor [8]. The ideal electrode material should possess large specific surface area, optimum pore size and size distribution, high electric conductivity, high chemical and thermal stability in electrolytes, and should have low-cost abundant supply.

ACs are generally produced from fossil-based hydrocarbons (e.g. coal and lignite [9, 10]) and biomass [11] (i.e. lignocellulosic materials [12]). At present coal is still the dominant raw material despite the environmental problems associated with its production and utilization [13]. Biomass, on the other hand, has been gaining popularity because of its distinctive advantages such as abundance and renewability. Various types of biomass have been used to produce ACs, including rice husks [14], coconut husks [15], cotton stalks [16], and most recently DDGS [17, 18]. A two-step method is generally used to make ACs: the raw materials are pyrolyzed to remove most of the non-carbon materials; the resultant char is activated to open pores [19]. Both physical and chemical methods are used in activation. In the physical method the activation occurs at elevated temperatures in the presence of oxidizing gases such as carbon dioxide or steam [20]. The chemical activation method combines carbonization and activation into one step, in which the raw materials are impregnated with activation agents (e.g. zinc chloride, phosphoric acid,

potassium hydroxide, etc.) and heated to a relatively low temperature for simultaneous carbonization and activation. Besides its simplicity and lower temperature requirement, chemical activation often results in much higher yields and better-developed pore structures [21].

Although ACs have been produced from different types of biomass, developing ACs from DDGS using energy-efficient microwave-induced heating has not been attempted. Microwave heating has the advantages of higher heating rate and lower energy cost. The goal of this study is to study the processing-property relationship of the DDGS-based ACs produced via microwave heating and phosphoric acid activation. Processing parameters including the acid/DDGS ratio and heating temperature are varied and their effects on the surface area, pore size and pore size distribution of the obtained ACs are determined. Great application potentials of the DDGS-based ACs are demonstrated through dye removal tests and supercapacitor applications.

Experimental

Materials

DDGS from Tharaldson Ethanol Plant (Casselton, North Dakota) was ground into powder and sieved through a 0.5 mm screen. The composition of DDGS was analyzed following the AOAC Official Methods [22]. The contents of neutral detergent fiber and acid detergent fiber were measured using an ANKOM Fiber Analyzer. Crude protein content was determined using a Tecator Kjeltac 1030 Autoanalyzer. Crude fat content was measured through ether extraction using a Goldfish fat extractor. The composition analysis shows that the as-received DDGS contains about 91 wt% dry matter, which comprises primarily fiber (~60 wt%), protein (~30 wt%) and fat (~10 wt%). Phosphoric acid (85 %, Baker) was used as the activation agent. Methylene blue (MB) (10 mg/mL in water, Alfa Aesar) was used as the adsorbate to test the adsorption behavior of the produced ACs. Conductive carbon black (TIMCAL SUPER C45), polyvinylidene fluoride (PVDF) binder and *N*-methyl-2-pyrrolidone (NMP) were purchased from MTI Corporation. All the chemicals in this study were used without further purification.

Preparation and Characterization of DDGS-Based ACs

DDGS was first impregnated with phosphoric acid at 1/1 and 2/1 acid/DDGS weight ratios. Distilled water was then added into the mixtures to lower their viscosity to enable magnetic stirring. The ratio of DDGS to distilled water was

set at 1:1 for all the samples. The stirring lasted for 1 h at 50 °C and homogeneous mixtures were formed at the end of the process. These precursors were then carbonized and activated using a microwave-assisted chemical activation method, in which the precursors were heat treated under different temperatures in a microwave furnace (CEM MAS 7000 Microwave Ashing Oven) for 20 min. After the treatment, the samples were cooled down to ambient temperature and washed with 0.5 M KOH solution and distilled water consecutively till the pH of the effluent was in the range of 6.0–7.0. A constant nitrogen flow of 1000 mL/min was supplied to the furnace during the entire heating and cooling process. The final AC products were obtained by drying the washed samples at 75 °C to a constant weight, followed by grinding and sieving them through a 500 mesh. The AC products were designated by their activation temperatures and acid/DDGS ratios. For example, the AC obtained at 300 °C with an acid/DDGS ratio of 2/1 was designated as AC-300-2. The surface morphology of the DDGS before and after the heat treatment was studied using SEM (JEOL JSM-6490LV). Energy-dispersive X-ray spectroscopy (EDS) was used to analyze the elements on the surface of the obtained ACs.

Specific Surface Area and Pore Size Distribution Measurements

The specific surface area, pore size and pore size distribution of the DDGS-based ACs were measured using an Accelerated Surface Area and Porosimetry System (ASAP2420, Micromeritics company) following the Brunauer–Emmett–Teller (BET) method and the density functional theory (DFT). Nitrogen was used as the adsorbate and the adsorption test was carried out at 77 K. Before the tests all the samples were heated to 160 °C at 10 °C/min under vacuum and kept isothermally for 240 min for degassing.

Adsorption Tests

To investigate the ACs' ability to remove dyes from water, 100 mg of selected ACs were added into 100 mL of MB solution (300 mg/L) in 125 mL Erlenmeyer flasks and all the flasks were shaken at 200 rpm using a Water Bath Orbital shaker (Thermo Scientific MaxQ 7000) at 50 °C. The concentrations of the MB solutions after different adsorption times were determined using a UV–Vis spectrophotometer (Varian Cary 5000, Agilent Technologies) by monitoring the intensity of the absorbance peak at 665 nm wavelength. A calibration curve was first obtained by measuring the intensities of the same peak of the MB solutions with known concentrations. In order to acquire adsorption equilibrium, 100 mg AC was added into 100 mL MB solution (300 mg/L) in a flask and the flask

was shaken (200 rpm at 50 °C) until the equilibrium was obtained (about 12 h). All the experiments were carried out without pH adjustment. The weights of MB adsorbed by each gram of ACs (i.e. adsorption ratio) at equilibrium (q_e) and at time t (q_t) were calculated by the following two equations, respectively.

$$q_e = \frac{C_0 - C_e}{W} V$$

$$q_t = \frac{C_0 - C_t}{W} V$$

where C_0 , C_t , and C_e are the initial MB mass concentration, the MB concentration at time t , and the MB concentration at equilibrium, respectively. V is the volume of the solution and W is the mass of the adsorbent.

Fabrication and Electrochemical Property Testing of Electrodes

To prepare supercapacitor electrodes using the DDGS-based ACs, the ACs, carbon black and polyvinylidene fluoride (PVDF) (80:10:10 by weight) were mixed and ground thoroughly. *N*-methyl-2-pyrrolidone (NMP) was added to the mixtures and pastes were formed after stirring. The pastes were then coated onto nickel foam current collectors, followed by drying in a vacuum oven overnight at 75 °C to remove NMP. The dried foams were pressed under a pressure of 10 MPa to ensure good electrical contacts between the ACs and the current collectors. The mass of the active materials (i.e. ACs, carbon black and PVDF) on the electrodes ranged from 5 to 12 mg.

The performance of the electrodes was analyzed at room temperature by cyclic voltammetry and chronopotentiometry tests using an electrochemical workstation (CHI 660C, CH Instruments, Inc.). A three-electrode cell was used for the tests with a platinum mesh as the counter electrode, Hg/HgO as the reference electrode, and 6 M KOH as the electrolyte, respectively. The voltammetry experiments were performed at different potential scan rates (5–100 mV/s) between 0 and -1 V. The specific capacitances (C_{sp}) were calculated from the obtained CV curves using the following equations: [8]

$$C_{sp} = \frac{\int i du}{2wv\Delta V}$$

where i and u are the instant current and instant potential, respectively. w is the mass of the active materials on the electrodes, v is the scan rate, and ΔV is the difference in voltage at the start and the end of a scan cycle.

The energy density (D_e) and power density (D_p) of the electrodes were calculated based on the galvanostatic charge/discharge (GCD) measurements performed between 0 and -1 V at various current densities (0.25–5 A/g):

$$D_e = \frac{1}{2} C_{sp} (\Delta V)^2$$

$$D_p = \frac{D_e}{\Delta t}$$

The specific capacitance was also calculated using:

$$C_{sp} = \frac{I \Delta t}{w \Delta V}$$

where I is the charge/discharge current, Δt is the time for a full discharging process, w is the mass of the active materials on the electrodes, and ΔV is the voltage window in the GCD tests. The electrochemical impedance spectroscopy (EIS) analysis was performed using a potentiostat (Gamry instruments, Reference 600) within the 0.01–20 K Hz frequency range under open circuit potential with a perturbation of 5 mV.

In-Situ Synthesis of MnO_2 During DDGS Carbonization

DDGS and phosphoric acid were first mixed at 1:1 ratio (total weight ~ 20 g). 15 mL $KMnO_4$ solution (100 mM)

was then added and the mixture was stirred for 30 min to form a homogenous slurry. The slurry was carbonized using a microwave oven at 600 °C under continuous nitrogen flow (1 L/min) for 20 min. The product was washed repeatedly using distilled water and fine black power was achieved after oven drying. The powder was made into electrodes and tested by the same methods as used on the pure ACs.

Results and Discussion

Surface Morphology Analysis

The optical and SEM images of the ground DDGS powder are shown in Fig. 1a, b, respectively. The sample exhibits spherical micro-grains with relatively smooth surface. After activation, the grainy structure disappears and a new nano-porous surface is presented (Fig. 1c). This dramatic change in structure is supposed to be caused by the oxidizing reaction with activation agents. This porous

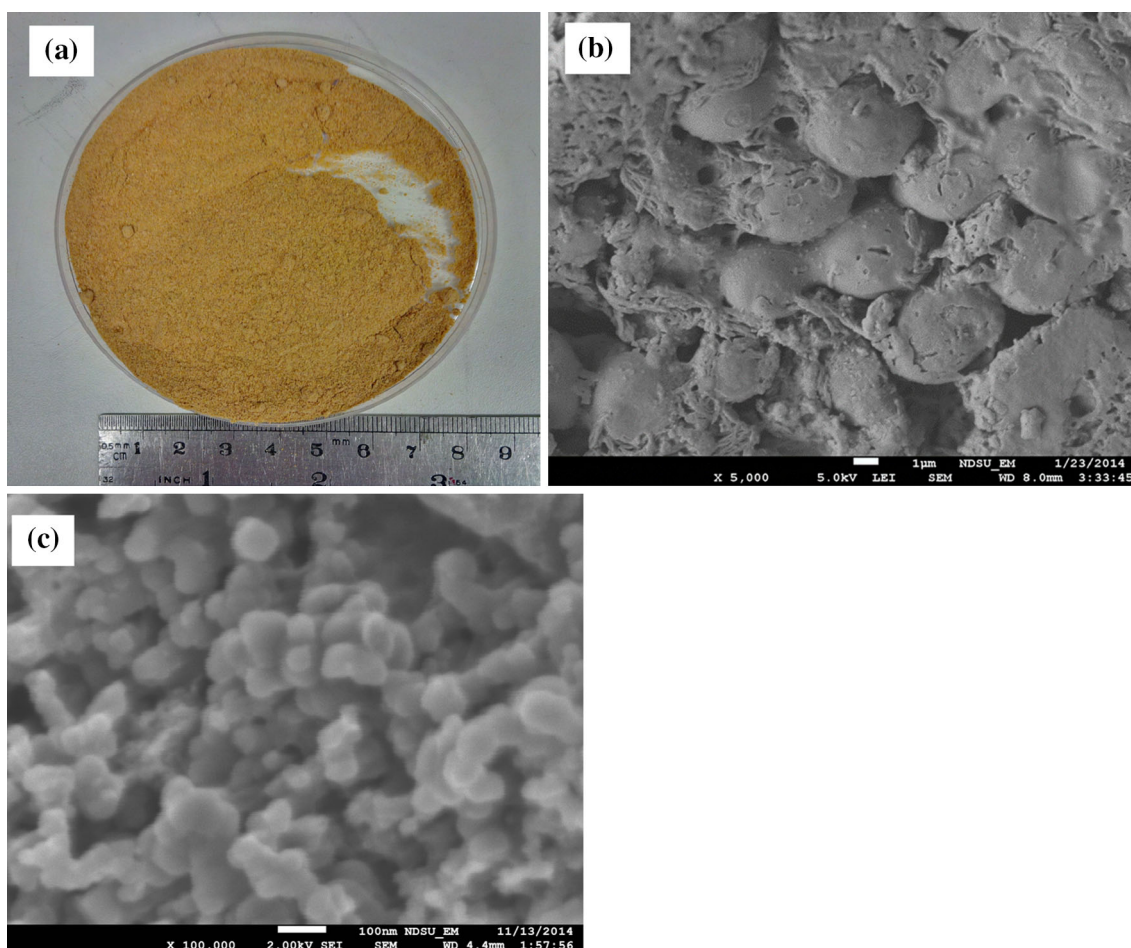


Fig. 1 Optical (a) and SEM (b) images of the ground DDGS powder. c The powder after microwave-induced activation

Table 1 Surface areas of the ACs prepared under different conditions

| Sample | Acid/DDGS ratio | Carbonization temperature | BET surface area (m ² /g) |
|----------|-----------------|---------------------------|--------------------------------------|
| AC-400-1 | 1:1 | 400 | 221.4 |
| AC-500-1 | 1:1 | 500 | 574.8 |
| AC-600-1 | 1:1 | 600 | 571.6 |
| AC-700-1 | 1:1 | 700 | 302.9 |
| AC-800-1 | 1:1 | 800 | 217.9 |
| AC-400-2 | 2:1 | 400 | 824.4 |
| AC-500-2 | 2:1 | 500 | 823.5 |
| AC-600-2 | 2:1 | 600 | 389.4 |
| AC-700-2 | 2:1 | 700 | 893.3 |
| AC-800-2 | 2:1 | 800 | 1035.8 |

structure can provide large surface area and allow high adsorption rate.

Surface Area and Pore Size Distribution

Surface area, pore size and pore size distribution of the DDGS-based ACs were calculated using Brunauer–Emmett–Teller (BET) theory and density functional theory (DFT) [23]. As shown in Table 1, the ACs exhibit a wide range of specific surface areas (217–1035 m²/g) with the maximum value achieved under the condition of 800 °C and 2:1 acid/DDGS ratio (i.e. sample AC-800-2). The results from Table 1 indicate that the development of porous structure is strongly affected by both the acid impregnation ratio and temperature. In general, high acid ratio leads to high surface area and there appears to be an optimal temperature for each acid ratio. The optimal temperature for impregnation ratio 1:1 is 500–600 °C, while for impregnation ratio 2:1 the largest surface area is achieved at 800 °C. This may be because with more activation agent, a higher temperature is needed for a complete reaction within the 20 min reaction time. After the reaction is completed, prolonged heating may enlarge the pores and therefore decrease the surface area. This explains the surface area decrease above 600 °C for the samples with 1:1 acid ratio. In order to study the effects of the surface area and pore size to dye adsorption and electrode capacitance, sample AC-600-1, AC-500-2 and AC-800-2 were chosen for further N₂ adsorption–desorption analysis, MB adsorption tests and electrochemical property tests. These three representative samples have a specific surface area of 571.6, 823.5 and 1035.8 m²/g, respectively. The samples with smaller surface areas were not tested because of their expected low performance in adsorption and electrochemical tests.

The N₂ adsorption–desorption isotherms of the three ACs (Fig. 2) exhibit features of both type I and type IV isotherms according to the BDDT (Brunauer–Deming–Deming–Teller) classification [24], which suggests that the

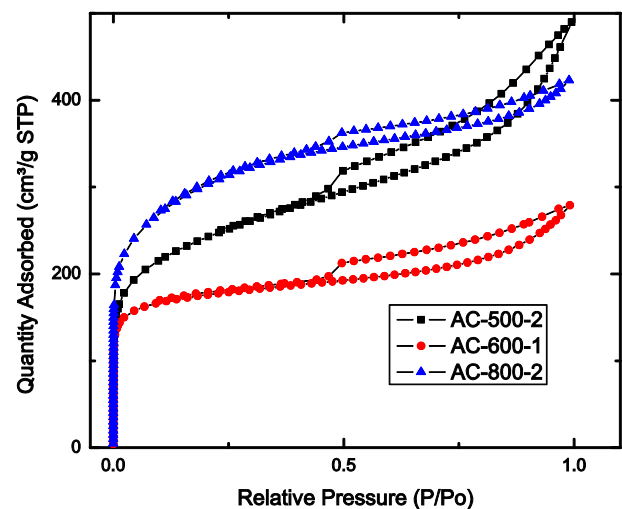


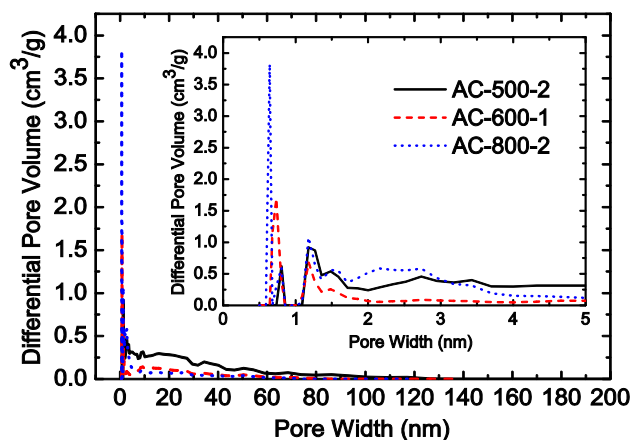
Fig. 2 N₂ adsorption–desorption isotherms at 77 K

ACs contain well-developed micropores (<2 nm) and mesopores (2–50 nm) [25]. It can be observed that at extremely low pressure (P/P_0 near 0), the isotherms show drastic adsorption and desorption, which is considered to be caused by the presence of ample micropores [26]. Besides, the occurrences of hysteresis loop under relatively high pressure ($0.5 < P/P_0 < 1$) indicate the existence of mesoporous structure [27]. The adsorption and desorption isotherms coincide at low pressure ($P/P_0 < 0.5$), suggesting that the uptake of nitrogen by the ACs materials with micropores is reversible.

The microstructures of the three ACs were further investigated using the DFT theory. The pore volume distribution determined by the DFT theory is given in Table 2, which indicates distinctive behaviors of the three samples. Comparing AC-800-2 with AC-500-2 (because their total pore volumes are close), the former has a much larger concentration of micropores (pores < 2 nm) and a smaller concentration of mesopores (2 nm < pores < 50 nm). Smaller pores give rise to larger surface areas when the

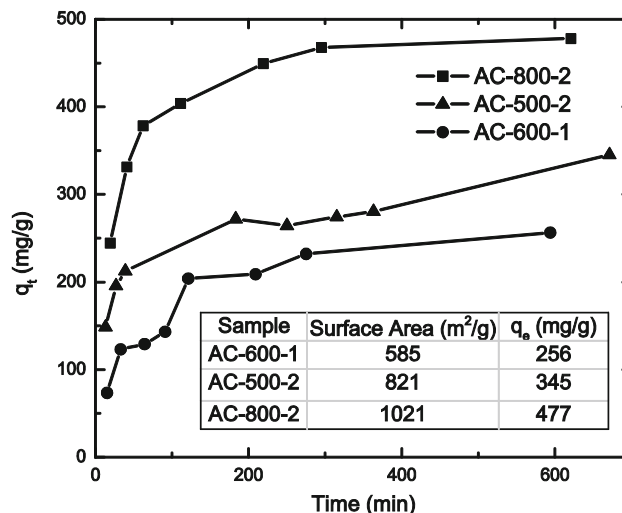
Table 2 Pore volume distributions of the three ACs based on DFT analysis

| Sample | Pore volume, volume percentage (cm ³ /g, %) | | | | Total |
|----------|--|---------|----------|--------|-------|
| | <2 nm | 2–10 nm | 10–50 nm | >50 nm | |
| AC-600-1 | 0.176 | 0.060 | 0.063 | 0.004 | 0.304 |
| | 58.2 % | 19.7 % | 20.8 % | 1.4 % | 100 % |
| AC-500-2 | 0.153 | 0.223 | 0.159 | 0.019 | 0.554 |
| | 27.7 % | 40.2 % | 28.8 % | 3.3 % | 100 % |
| AC-800-2 | 0.299 | 0.165 | 0.040 | 0.002 | 0.506 |
| | 58.9 % | 32.4 % | 8.1 % | 0.5 % | 100 % |

**Fig. 3** Pore size distribution from DFT analysis of the three samples. The inset shows the distribution below 5 nm

volumes are equal, which explains AC-800-2's larger surface area. Previous research shows that micropores develop better at a higher heating rate and as a result, the micropore volume and the specific surface area increase [28, 29]. The heating rate is high in this study due to the use of microwave heating, thus facilitating the creation of micropores in general. The higher acid/DDGS ratio in AC-800-2 caused a larger scale of acid-carbon reaction during the activation process, and therefore more micropores were created.

The pore size distribution diagrams of the three ACs are shown in Fig. 3, which agree with the pore characteristics given by Table 2. It is obvious from the figure that AC-500-2 has substantially higher distribution in the mesopore region than the other two samples. This higher distribution also corresponds closely to the larger isotherm hysteresis loop of AC-500-2 (Fig. 2). The inset of Fig. 3 shows the distribution of the pores within the 5 nm range, which clearly indicates higher concentrations of the micropores (especially those below 1 nm) in AC-600-1 and AC-800-2. The different surface areas and pore size distributions of the three ACs are expected to cause different results in dye removal and electrochemical tests, as is discussed below.

**Fig. 4** MB adsorption as a function of time for the three ACs

MB Adsorption

Figure 4 shows MB adsorption ratio as a function of adsorption time for the three ACs. All the samples show high-rate adsorption within the first 30 min, followed by second-stage low-rate adsorption and eventual equilibrium at the end of the experiments. Clearly, the adsorption capacity (i.e. the adsorption ratio at equilibrium) increases with increasing surface area of the ACs because more surface area is available for dye molecule absorption.

Several thermodynamic models have been used to simulate the adsorption process and they can offer important process information (e.g. equilibrium concentration) when the equilibrium is reached [30]. On the contrary, a kinetic analysis focuses on the changes in chemical properties with time as well as the rates of the changes. A pseudo-first-order kinetic model was used in this study to further understand the adsorption behavior of the ACs. In this model the mass action rate of a chemical phenomenon and the diffusion through a boundary liquid film assume the pseudo-first-order rate equation devised by Lagergren [31],

$$\log(q_e - q_t) = \log q_e - kt$$

where q_e and q_t are the amounts of dye adsorbed at time t and at equilibrium, respectively [32]. k is the pseudo-first-order rate constant of adsorption. As shown in Fig. 5, the plots of $\log(q_e - q_t)$ versus time for the three ACs exhibit relatively linear relationships, and this linearity confirms that the adsorption process is governed by the first-order kinetics. Figure 5 demonstrates the applicability of the pseudo-first-order kinetic model and therefore it can be used to predict ACs' adsorption behavior. The $|k|$ values for the three ACs follow the order of AC-800-2 > AC-500-

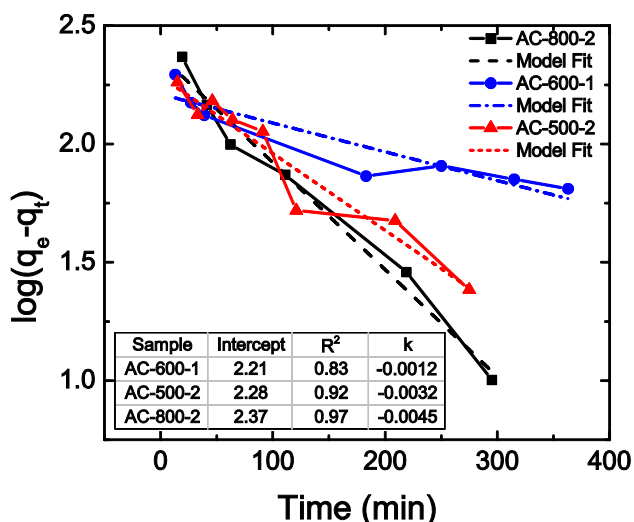


Fig. 5 Pseudo-first-order kinetic model simulation for the MB adsorption of the ACs

2 > AC-600-1, which agrees with the adsorption rate/capacity results given in Fig. 4.

Electrochemical Analysis

Figure 6 shows the CV plots of the electrodes made with the three ACs. The scan rate was set at 10 mV/s for all the tests. The near-rectangular shape of the CV curves indicates a well-defined EDLC behavior. The table inset in Fig. 6 shows that despite the fact that sample AC-800-2 has the largest surface area, it only exhibits a medium specific capacitance. Although large surface area is generally considered to benefit the specific capacitance, pore size and its distribution play equally, if not more, important roles in determining the capacitance (and so the energy storage capability) of an electrode. Indeed, some studies have shown that the ACs with small pore size and narrow pore size distribution tend to have reduced specific capacitance [13]. During the charge/discharge process, micropores primarily act as the ion traps for charge storage while the mesopores play dual roles: offering surface for ion adsorption and forming pathways for ion transport [33]. Both micropores and mesopores are critical in achieving large capacitance and high-energy storage. Comparing AC-800-2 with AC-500-2, the former has larger total surface area but much smaller percentage of mesopores (Table 2). This smaller percentage can lead to lack of adequate pathways for ion transport, thus hindering the charge/discharge process. As a result, the capacitance of AC-800-2 is reduced.

To study the electrochemical properties of the electrodes under different scan rates and current densities, AC-500-2 (the sample with the highest capacitance) was chosen for

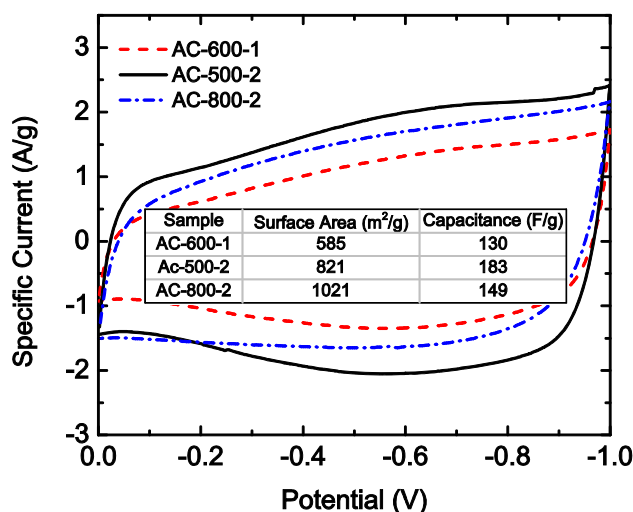


Fig. 6 CV plots of the three ACs at the scan rate 10 mV/s. The inset gives the surface area and capacitance calculated based on the plots for the three samples

further characterization. Figure 7a shows its CV curves under twelve different scan rates (up to 100 mV/s) in 6 M KOH aqueous solutions. A quasi-rectangular shape for a CV curve indicates a perfect electrical double-layer capacitance performance with fast charge/discharge rates. The figure demonstrates that the curves of AC-500-2 can retain their quasi-rectangular shapes relatively well up to 50 mV/s, indicating the electrode’s pure EDLC behavior and its capability to rapidly forming the double-layer even at high scan rates. The CV plots do severely deviate from their original quasi-rectangular shapes at very high scan rates (>50 mV/s) and their corresponding capacitances decrease as a result (Fig. 7b). The decrease is considered to be caused by the nonzero time constant and elevated transient current, which lead to a longer charge/discharge time and thus the deviations [34]. Specific capacitance of the electrode can be calculated based on the plots using the equation $C_{sp} = \frac{\int idu}{2w\Delta V}$. Depending on the scan rate, the capacitance values ranging from 120 to 210 F/g are obtained, with the highest one being achieved at the scan rate of 5 mV/s [35, 36]. According to previous studies, the state of the art EDLCs using ACs or other nanocomposites as electrodes show a typical specific capacitance of 100–200 F/g [37, 38]. Therefore our results demonstrate that the DDGS-based ACs is a promising electrode material for the development of high capacity EDLCs.

Galvanostatic charge/discharge (GCD) experiments were performed at different current densities (0.25–5.0 A/g) in order to assess the energy and power characteristics of the DDGS-based electrodes (Fig. 7c). The results reveal that the potential-time curves for all the current densities are isosceles triangles, indicating ideal EDLC behavior, which

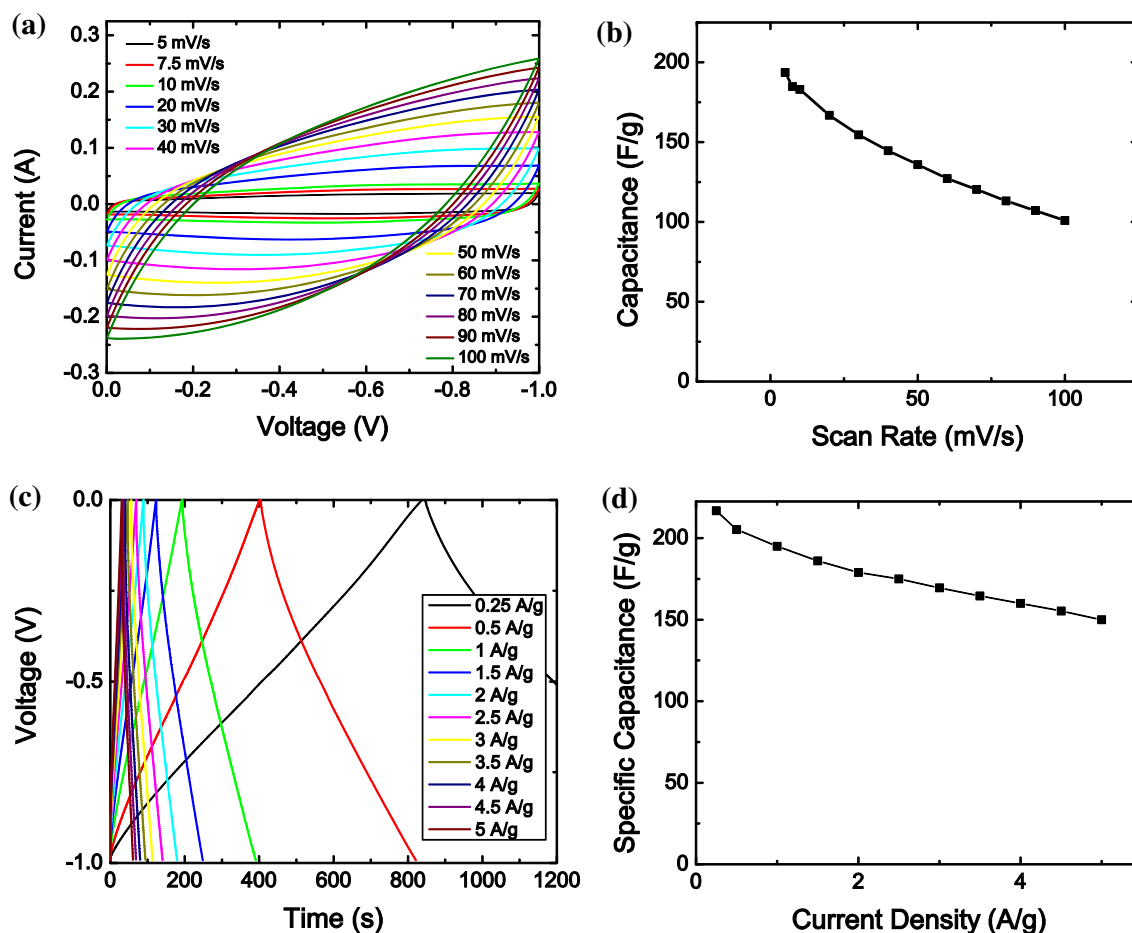


Fig. 7 **a** CV plots of AC-500-2 at different scan rates. **b** Specific capacitance versus scan rate of AC-500-2. **c** GCD plots for AC-500-2 at different current densities. **d** Specific capacitance versus current density for the same sample

confirms the results obtained by cyclic voltammetry. Moreover, no discernible internal resistance (IR) drop can be found on both the charge and discharge curves at even the highest current density, suggesting low energy dissipation of the capacitor. The capacitances calculated from the GCD tests are in good accordance with the values derived from the CV tests, ranging from 217 to 150 F/g with the maximum acquired at the current density of 0.25 A/g. As shown by the Fig. 7d, C_{sp} of the electrode decreases slightly with increasing current density, which can be explained by the fact that at low current densities the electrolyte ions have adequate time to diffuse into the nano-sized pores in the electrode, while at high current densities the process of diffusion cannot be done completely and hence a decrease in the corresponding capacitance is resulted.

The DDGS-based electrodes also show excellent durability. In Fig. 8a after 1000 cycles of charge–discharge at current density of 1 A/g, the system still retains nearly 99 % of its initial capacitance, showing that the material has great stability even at strong alkali environments.

Ragone plots are widely used to evaluate the performance of energy storage devices by plotting energy density versus power density [39]. To investigate the practical function of the prepared electrodes, the energy density and power density were calculated at different current densities according to the equations $D_e = \frac{1}{2} C_{sp} (\Delta V)^2$ and $D_p = \frac{D_e}{\Delta t}$ and the results are plotted in Fig. 8b, which shows that the working electrode exhibits high power densities up to 2500 W/kg, which exceeds the performance of the mesoporous carbon nanotube-based electrodes (2000 W/kg) [40] and Ni_3S_2 nanosheet array-based electrodes (1500 W/kg) [41] developed by other researchers. As a comparison, conventional batteries such as lithium ion batteries can currently reach a power density around 100 W/kg [42]. This large difference is caused by their different energy storage mechanisms. EDLCs have the advantages of high power density and rapid charge/discharge due to the reason that the energy stored in a capacitor is by the form of electron field instead of chemical reactions, and the mobility of electrons is much larger than that of lithium ions or any other redox couples.

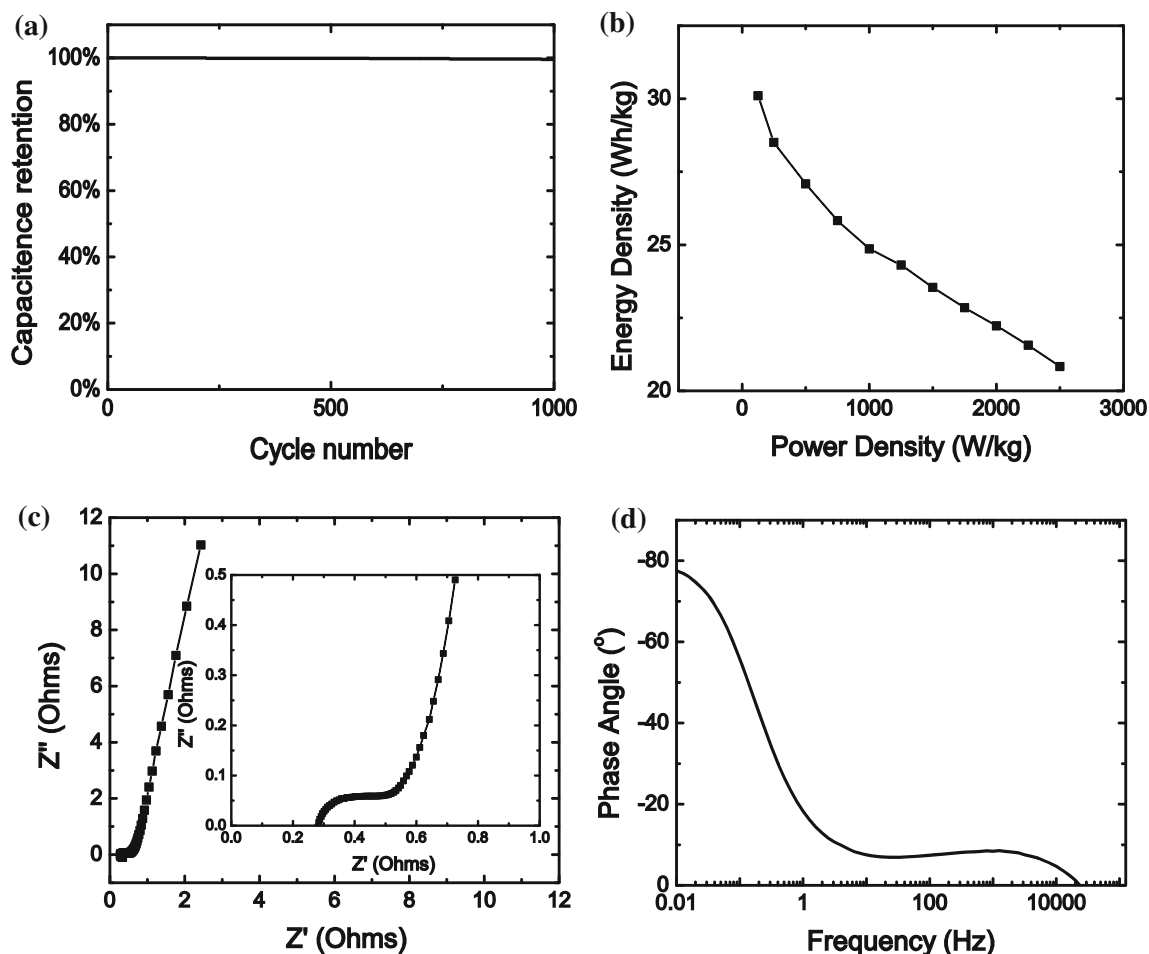


Fig. 8 **a** Capacitance retention over 1000 cycles. **b** Ragone plot at different current densities. **c** Nyquist plot of the working electrode. **d** Bode plot of the working electrode. All the results are for AC-500-2

The electrochemical impedance spectroscopy (EIS) analysis provides additional evaluation on EDLCs' electrochemical performance, such as its frequency dependence and equivalent series resistance (ESR). It is one of the principal methods used for EDLC testing. The EIS analysis in this study was carried out from 0.01 to 10^5 Hz at open circuit potential with a perturbation of 5 mV. As shown by the complex-plane (Nyquist) impedance plot presented in Fig. 8c, the impedance spectrum is composed of a semi-circle section with a small radius in the high-frequency region, followed by a straight line in the low-frequency region. At low frequencies, the spectrum approaches 90° with respect to the real axis due to the strong capacitive behavior of the electrode. The spectrum intersects with the real axis at a $\sim 45^\circ$ angle at high frequencies. This type of spectrum can be explained by a series resistor–capacitor (RC) model in which an ideal capacitor is connected with a serial resistance (ESR). In the impedance phase angle—frequency plot (Bode plot, Fig. 8d), at low frequencies, the working electrode behaves like an ideal capacitor with a

phase angle near 90° , but at high frequencies, the resistive component dominates and the phase angle is reduced to nearly 10° , which renders the working electrode resistor-like behavior. This phenomenon is considered to be caused by reduced pore penetration depth at high frequencies, which results in less fraction of pores taking part in the charge/discharge process [43].

Pseudocapacitance of the DDGS-Based ACs

MnO_2 is widely recognized as one of the most suitable materials to make electrodes with high pseudocapacitance because of its high theoretical specific capacitance (1370 F/g) [44], low cost and low environmental impact [45]. Pseudocapacitance is based on the Faradaic redox reactions during charging/discharging processes, which often result in a specific capacitance several times higher than that of electrostatic double-layer capacitance. The mechanism of the redox reaction/charge storage for MnO_2 can be described as follows [44]:

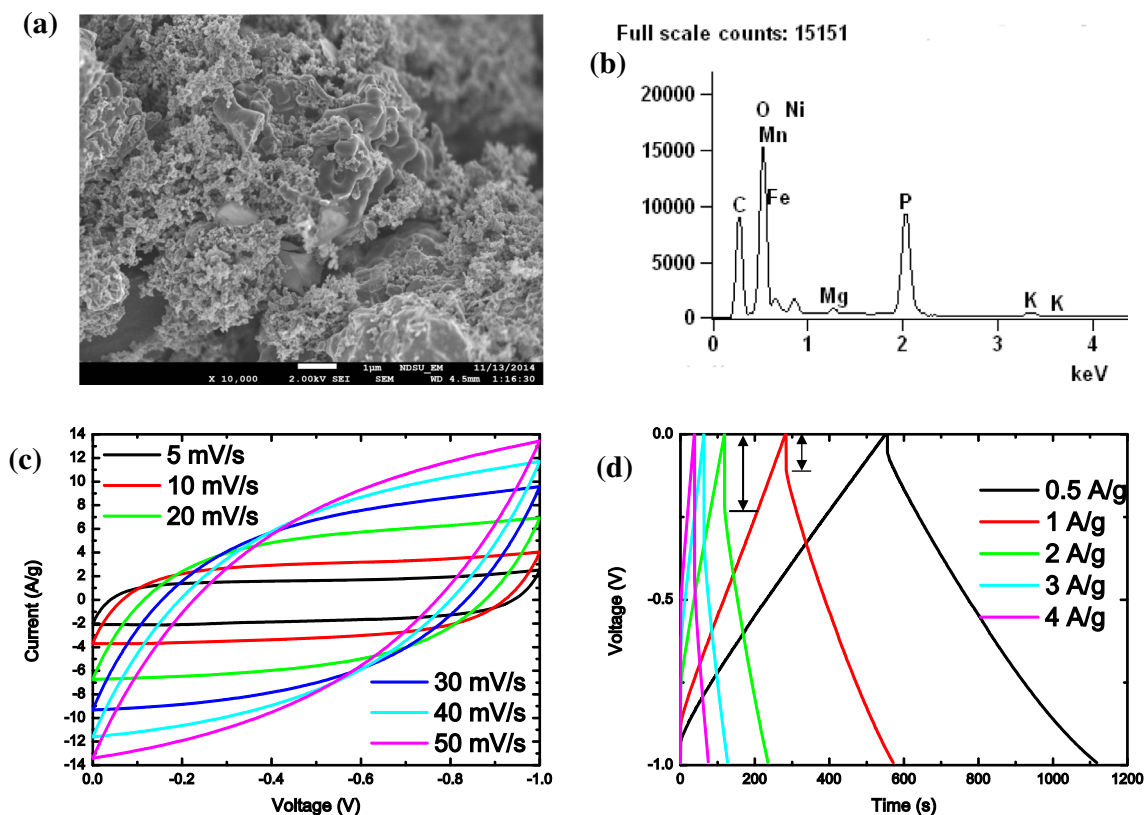
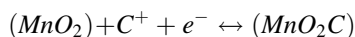
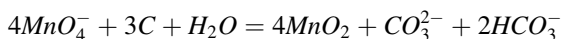


Fig. 9 **a** SEM picture of in situ synthesized MnO₂ particles on AC. **b** EDS counts on a selected area of the SEM. **c** CV plots of AC/MnO₂ electrode at different scan rates. **d** GCD plots for AC/MnO₂ at

different current densities. *Arrows* indicate the IR drops when the current direction changes



where C⁺ denotes electrolyte cations such as Li⁺, Na⁺, K⁺. The specific capacitance of the DDGS-based ACs in this study was further increased by in situ synthesis of MnO₂ during AC production. The MnO₂ was formed by the reaction between carbon and KMnO₄, which can be described as follows in a pH neutral solution [46]:



In Fig. 9a the formed MnO₂ particles are seen widely distributed on the surface of ACs. The energy dispersive X-ray spectroscopy (EDS) results confirms the existence of Mn (Fig. 9b). The CV and GCD test results for the AC/MnO₂ electrode under different voltage scan rates and current rates are shown in Fig. 9c, d, respectively. Based on the two figures, the highest specific capacitance was calculated to be 296.8 F/g (at 10 mV/s) from the CV test and 285.7 F/g (at 1 A/g) from the GCD test. These values are about 1/3 higher than those of the pure ACs, highlighting the significant contribution from the pseudocapacitive behavior of MnO₂. It should be pointed out that noticeable IR drops can be observed from Fig. 9d, which is

most likely due to the relatively low electrical conductivity of MnO₂ [45].

Conclusion

In this research we developed a one-step facile method to produce 3D porous ACs from DDGS using a microwave-assisted chemical activation method. The surface area of the obtained ACs varied from several hundreds to the maximum of nearly 1036 m²/g, depending on the acid ratio and the activation temperature. Pore size analysis found that the ACs contained large fraction of micropores. MB adsorption tests showed that the adsorption capacity of the ACs was proportional to their surface areas, with the highest being 477 mg/g for the 1036 m²/g surface area. The EDLCs based on the DDGS-based ACs exhibited excellent electrochemical performance and stability. The specific capacitances ranging from 120 to 210 F/g were achieved and the electrode showed minimal degradation after 1000 charge/discharge cycles. The specific capacitance can be further improved up to nearly 300 F/g by forming AC/MnO₂ composite with pseudocapacitance

behavior. The adsorption and electrochemical test results indicated that the adsorption capacity was determined by the total surface area of the ACs, while the capacitance was critically controlled by both the surface area and the pore size distribution. This study demonstrated the potentials of DDGS in environmental remediation and energy storage applications.

Acknowledgments The authors would like to thank Jessica Latimer for the training of the microwave furnace and Drs. Yechun Wang and Qixin Zhou for their assistance to the EIS experiment. The authors also gratefully thank Guofeng Ren from Texas Tech University for helpful and enlightening discussion.

Compliance with Ethical Standards

Funding Research funds from North Dakota Corn Council and King Abdullah University of Science and Technology Baseline are greatly appreciated.

Conflict of interest The authors declare no competing financial interest.

References

- Kim Y, Mosier NS, Hendrickson R et al (2008) *Bioresour Technol* 99:5165
- Stein HH, Shurson GC (2009) *J Anim Sci* 87:1292
- Wang X, Liang X, Wang Y et al (2011) *Desalination* 278:231
- Sharma YC, Uma (2009) *J Chem Eng Data* 55:435
- Berrios M, Martín MÁ, Martín A (2012) *J Ind Eng Chem* 18:780
- Vijayaraghavan K, Balasubramanian R (2013) *J Environ Chem Eng* 1:473
- Kötz R, Carlen M (2000) *Electrochim Acta* 45:2483
- Zhang LL, Zhao XS (2009) *Chem Soc Rev* 38:2520
- Maldhure AV, Ekhe JD (2011) *Chem Eng J* 168:1103
- Yagmur E, Tunc MS, Banford A, Aktas Z (2013) *J Anal Appl Pyrol* 104:470
- Foo KY, Hameed BH (2011) *Bioresour Technol* 102:9794
- Foo KY, Hameed BH (2011) *Chem Eng J* 166:792
- Zhao X-Y, Huang S-S, Cao J-P et al (2014) *J Anal Appl Pyrol* 105:116
- Guo Y, Zhao J, Zhang H et al (2005) *Dyes Pigm* 66:123
- Tan IAW, Ahmad AL, Hameed BH (2008) *Chem Eng J* 137:462
- Deng H, Zhang G, Xu X, Tao G, Dai J (2010) *J Hazard Mater* 182:217
- Jin H, Wang X, Gu Z (2013) *Mater Focus* 2:497
- Hong J, Xiaomin W, Zhengrong G (2013) *Mater Focus* 2:105
- Ioannidou O, Zabaniotou A (2007) *Renew Sustain Energy Rev* 11:1966
- Bouchelta C, Medjram MS, Bertrand O, Bellat J-P (2008) *J Anal Appl Pyrol* 82:70
- Zhong Z-Y, Yang Q, Li X-M, Luo K, Liu Y, Zeng G-M (2012) *Ind Crops Prod* 37:178
- Horwitz W, Latimer GW (2005) *Official methods of analysis of AOAC International*. AOAC International, Gaithersburg
- Figueroa-Gerstenmaier S, Bonet Avalos J, Gelb LD, Gubbins KE, Vega LF (2003) *Langmuir* 19:8592
- Gañán J, González-García CM, González JF, Sabio E, Macías-García A, Díaz-Díez MA (2004) *Appl Surf Sci* 238:347
- Rodríguez-Reinoso F, Martín-Martínez JM, Prado-Burgete C, McEnaney B (1987) *J Phys Chem* 91:515
- Sevilla M, Parra JB, Fuertes AB (2013) *ACS Appl Mater Interfaces* 5:6360
- Groen JC, Peffer LAA, Pérez-Ramírez J (2003) *Micropor Mesopor Mater* 60:1
- Fu P, Hu S, Xiang J, Sun L, Su S, Wang J (2012) *J Anal Appl Pyrol* 98:177
- Moreno AH, Arenillas A, Calvo EG, Bermúdez JM, Menéndez JA (2013) *J Anal Appl Pyrol* 100:111
- Liu L, Lin Y, Liu Y, Zhu H, He Q (2013) *J Chem Eng Data* 58:2248
- Boyd GE, Adamson AW, Myers LS (1947) *J Am Chem Soc* 69:2836
- Wang S, Zhu ZH, Coomes A, Haghseresht F, Lu GQ (2005) *J Colloid Interface Sci* 284:440
- Zhi M, Xiang C, Li J, Li M, Wu N (2013) *Nanoscale* 5:72
- Prabaharan SRS, Vimala R, Zainal Z (2006) *J Power Sources* 161:730
- Xu B, Wu F, Chen R et al (2008) *Electrochem Commun* 10:795
- Wang D-W, Li F, Liu M, Lu GQ, Cheng H-M (2008) *Angew Chem Int Ed* 47:373
- Lu W, Hartman R, Qu L, Dai L (2011) *J Phys Chem Lett* 2:655
- Lei C, Amini N, Markoulidis F, Wilson P, Tennison S, Lekakou C (2013) *J Mater Chem A* 1:6037
- Yan J, Fan Z, Wei T et al (2009) *J Power Sources* 194:1202
- Jiang H, Li C, Sun T, Ma J (2012) *Nanoscale* 4:807
- Huo H, Zhao Y, Xu C (2014) *J Mater Chem A* 2:15111
- Wei D, Scherer MRJ, Bower C, Andrew P, Ryhänen T, Steiner U (2012) *Nano Lett* 12:1857
- Wang G, Zhang L, Zhang J (2012) *Chem Soc Rev* 41:797
- Toupin M, Brousse T, Bélanger D (2004) *Chem Mater* 16:3184
- Wei W, Cui X, Chen W, Ivey DG (2011) *Chem Soc Rev* 40:1697
- Jin X, Zhou W, Zhang S, Chen GZ (2007) *Small* 3:1513